ATLAS CONF Note

ATLAS-CONF-2023-064

26th September 2023

Search for non-resonant Higgs boson pair production in the $2b + 2\ell + E_{\mathrm{T}}^{\mathrm{miss}}$ final state in pp collisions at $\sqrt{s} = 13$ TeV with the ATLAS detector

The ATLAS Collaboration

A search for non-resonant Higgs boson pair (HH) production is presented, in which one of the Higgs bosons decays to a b-quark pair ($b\bar{b}$) and the other decays to WW^*, or ZZ^*, or $\tau^+\tau^-$, with in each case a final state with $\ell^+\ell^-$+ neutrinos ($\ell = e, \mu$). Both gluon-gluon fusion and vector boson fusion are considered as production modes. Data recorded by the ATLAS detector in proton-proton collisions at a centre-of-mass energy of 13 TeV at the Large Hadron Collider, corresponding to an integrated luminosity of 140 fb^{-1}, are used in this analysis. Events are selected to have exactly two b-tagged jets and two leptons with opposite electric charge and missing transverse momentum in the final state. These events are classified using multivariate analysis algorithms to separate the HH events from other Standard Model processes. No evidence of the signal is found. The observed (expected) upper limit on the cross-section for non-resonant Higgs boson pair production is determined to be 9.6 (16.2) times the Standard Model prediction at 95% confidence level. Likelihood scans for the Higgs boson self-interaction coupling parameter κ_λ and the quadrilinear coupling parameter κ_{2V} are also performed in this analysis, constraining these parameters to be within the ranges $[-6.2, 13.3]$ and $[-0.17, 2.4]$, respectively, at 95% confidence level.

ATLAS-CONF-2023-064
02 October 2023

1 Introduction

The Standard Model (SM) of particle physics employs the Higgs mechanism [1–6] to formulate a theoretical model in which the weak gauge bosons (W, Z) and the fermions acquire mass. Following the discovery of the Higgs boson, referred to as H, by the ATLAS and CMS collaborations [7, 8] at the Large Hadron Collider (LHC) in 2012, one of the remaining open questions is about the structure of the Higgs potential which is still largely unconstrained. The rate of the double Higgs production (HH) process is sensitive to the trilinear Higgs self-interaction coupling λ_3, i.e. the coupling describing a vertex with three Higgs bosons interacting with one another. It is common practice to define a Higgs boson trilinear coupling modifier as the actual trilinear coupling value divided by its SM expectation value: $\kappa_\lambda \equiv \lambda_3/\lambda_3^{SM}$.

The dominant HH production process at the LHC is through gluon-gluon fusion (ggF), which involves either a top-quark box-loop (also referred to as *box-diagram*) or decay of an off-shell Higgs boson (also referred to as *triangle-diagram*) at lowest order; the Feynman diagrams are shown in Figures 1(a) and 1(b) respectively. The *box-diagram* and *triangle-diagram* interfere destructively, leading to a small cross-section for the $gg \to HH$ processes, $\sigma_{\text{ggF}} = 31.05^{+6.7\%}_{-23.2\%}$ fb, calculated at the next-to-next-to-leading order (NNLO) and including finite top-quark mass effects for a Higgs boson mass of $m_H = 125$ GeV [9–16].

The vector-boson-fusion (VBF) process is the sub-leading Higgs boson pair production mode, with a cross-section of $\sigma_{\text{VBF}} = 1.726 \pm 2.1\%$ fb calculated at N^{3}LO QCD for a Higgs boson mass of $m_H = 125$ GeV [17]. The VBF HH production is not only sensitive to κ_λ but also depends on the coupling modifier of the Higgs boson to vector bosons (κ_V) and on another coupling modifier related to the quartic vertex involving two vector bosons and two Higgs bosons (κ_{2V}). The corresponding diagrams are shown in Figure 2.

In the presence of beyond SM (BSM) physics, the HH production cross-section can be altered by modifying the value of the self-coupling λ_3, leading to values for κ_λ different from the SM prediction as discussed in Refs. [18, 19]. Similarly, modifications of the coupling to vector bosons can alter κ_{2V}. Probing the Higgs boson self-coupling can therefore provide additional information about the validity of the SM.

Searches for SM HH production through the decay channels $HH \to bb\gamma\gamma$ [20], $HH \to 4b$ [21] and $HH \to bb\tau\tau$ [22] were performed using the full Run-2 dataset collected by the ATLAS experiment at $\sqrt{s} = 13$ TeV. The results from these three channels have been combined [23] to improve the search sensitivity. The observed (expected in the absence of HH production) combined upper limit on the production rate of SM Higgs boson pairs, at the 95% confidence level (CL), was found to be 2.4 (2.9) times the SM prediction. The value of κ_λ was constrained to be within the observed (expected) range $[-0.6, 6.6]$ ($[-2.1, 7.8]$) at 95% CL and the value for κ_{2V} was constrained to be within the observed (expected) range

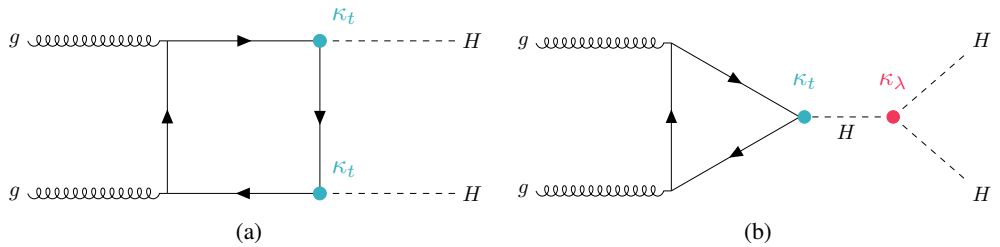

Figure 1: The LO Feynman diagrams for the gluon-gluon fusion process of Higgs boson pair production at the LHC, where κ_λ denotes the Higgs boson trilinear coupling modifier $\kappa_\lambda \equiv \lambda_3/\lambda_3^{SM}$ and κ_t the coupling modifier relative to the top-quark-Higgs-boson coupling.

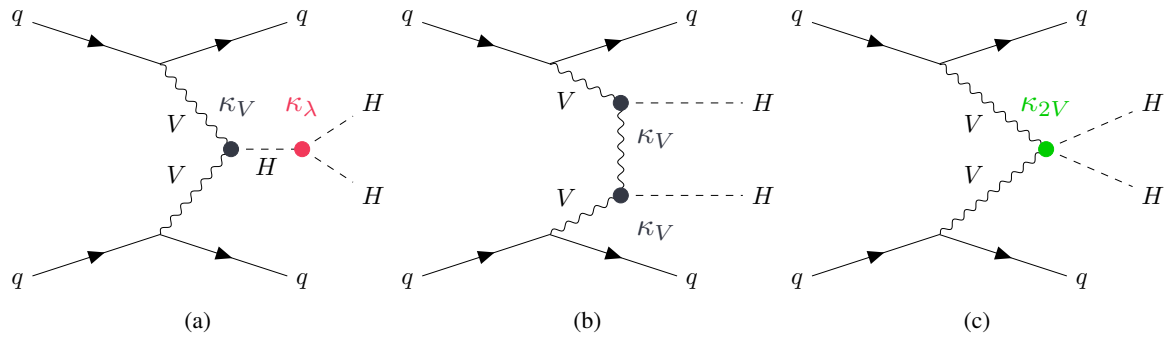

Figure 2: The LO Feynman diagrams for the vector-boson-fusion process of Higgs boson pair production, where κ_λ, κ_V, and κ_{2V} are the coupling modifiers related to HHH, HVV, and $HHVV$ vertices.

$[0.1, 2.0]$ ($[0.0, 2.1]$) at 95% CL [23]. Similar results have also been obtained by the CMS experiment; according to those results, κ_λ is constrained to be within the observed range of $[-1.2, 6.5]$ at 95% CL [24] and κ_{2V} is constrained to be within the observed range of $[-0.67, 1.4]$ at 95% CL [24].

This note focuses on a data analysis using $2b + 2\ell + E_{\mathrm{T}}^{\mathrm{miss}}$ ($\ell = e, \mu$) final states arising from different HH decay channels,

$$HH \to b\bar{b} + WW^*/ZZ^*/\tau^+\tau^- \to b\bar{b} + \ell^+\ell^- + \text{neutrinos},$$

with one of the Higgs bosons decaying to b-quark pair ($b\bar{b}$) and the other decaying to a boson (WW^*, ZZ^*) or a $\tau^+\tau^-$ pair, which furthers decay to $\ell^+\ell^-$ + neutrinos. The experimental signature is characterised by two b-tagged jets with the invariant mass m_{bb} close to m_H, two charged leptons with opposite charges, and large missing transverse energy $E_{\mathrm{T}}^{\mathrm{miss}}$ due to neutrinos escaping detection. The decay channel with a Higgs boson decaying to two Z bosons and the subsequent final state with two leptons and two quark-initiated jets from the ZZ system, $bbZZ \to bb2\ell2q$ is also considered. Although this final state does not have $E_{\mathrm{T}}^{\mathrm{miss}}$ due to presence of neutrinos, it can have $E_{\mathrm{T}}^{\mathrm{miss}}$ due to detector and reconstruction in-efficiencies. Dominant background arises from top-quark processes ($t\bar{t}$, Wt and $t\bar{t}V$ with $V = W, Z$), and production of a Z boson associated with heavy-flavour jets (Z+HF). The search uses the full Run 2 dataset collected with the ATLAS experiment in proton-proton (pp) collisions at 13 TeV, corresponding to a total integrated luminosity of 140 fb^{-1}.

A search for HH production in the $2b + 2\ell + E_{\mathrm{T}}^{\mathrm{miss}}$ final state considering only $HH \to bbWW^*$ using the full Run-2 dataset has already been performed [25]; the work presented in this note significantly improves the analysis techniques by optimizing a deep neural network (DNN) to better classify the $2b + 2\ell + E_{\mathrm{T}}^{\mathrm{miss}}$ events into HH signal or background and considers additional decay channels, leading to a factor two better sensitivity. Furthermore, studies of HH production through the VBF process are included for the first time in the $2b + 2\ell + E_{\mathrm{T}}^{\mathrm{miss}}$ final state. In addition, the compatibility of the data with non-SM values of the κ_λ and κ_{2V} parameters is constrained in this note.

2 ATLAS detector

The ATLAS detector [26] at the LHC covers nearly the entire solid angle around the collision point.[1] It consists of an inner tracking detector surrounded by a thin superconducting solenoid, electromagnetic and hadron calorimeters, and a muon spectrometer incorporating three large superconducting air-core toroidal magnets.

The inner-detector system (ID) is immersed in a 2 T axial magnetic field and provides charged-particle tracking in the range $|\eta| < 2.5$. The high-granularity silicon pixel detector covers the vertex region and typically provides four measurements per track, the first hit normally being in the insertable B-layer (IBL) installed before Run 2 [27, 28]. It is followed by the silicon microstrip tracker (SCT), which usually provides eight measurements per track. These silicon detectors are complemented by the transition radiation tracker (TRT), which enables radially extended track reconstruction up to $|\eta| = 2.0$. The TRT also provides electron identification information based on the fraction of hits (typically 30 in total) above a higher energy-deposit threshold corresponding to transition radiation.

The calorimeter system covers the pseudorapidity range $|\eta| < 4.9$. Within the region $|\eta| < 3.2$, electromagnetic calorimetry is provided by barrel and endcap high-granularity lead/liquid-argon (LAr) calorimeters, with an additional thin LAr presampler covering $|\eta| < 1.8$ to correct for energy loss in material upstream of the calorimeters. Hadron calorimetry is provided by the steel/scintillator-tile calorimeter, segmented into three barrel structures within $|\eta| < 1.7$, and two copper/LAr hadron endcap calorimeters. The solid angle coverage is completed with forward copper/LAr and tungsten/LAr calorimeter modules optimised for electromagnetic and hadronic energy measurements respectively.

The muon spectrometer (MS) comprises separate trigger and high-precision tracking chambers measuring the deflection of muons in a magnetic field generated by the superconducting air-core toroidal magnets. The field integral of the toroids ranges between 2.0 and 6.0 T m across most of the detector. Three layers of precision chambers, each consisting of layers of monitored drift tubes, cover the region $|\eta| < 2.7$, complemented by cathode-strip chambers in the forward region, where the background is highest. The muon trigger system covers the range $|\eta| < 2.4$ with resistive-plate chambers in the barrel, and thin-gap chambers in the endcap regions.

Interesting events are selected by the first-level trigger system implemented in custom hardware, followed by selections made by algorithms implemented in software in the high-level trigger [29]. The first-level trigger accepts events from the 40 MHz bunch crossings at a rate below 100 kHz, which the high-level trigger further reduces in order to record events to disk at about 1 kHz.

An extensive software suite [30] is used in data simulation, in the reconstruction and analysis of real and simulated data, in detector operations, and in the trigger and data acquisition systems of the experiment.

[1] ATLAS uses a right-handed coordinate system with its origin at the nominal interaction point (IP) in the centre of the detector and the z-axis along the beam pipe. The x-axis points from the IP to the centre of the LHC ring, and the y-axis points upwards. Cylindrical coordinates (r, ϕ) are used in the transverse plane, ϕ being the azimuthal angle around the z-axis. The pseudorapidity is defined in terms of the polar angle θ as $\eta = -\ln\tan(\theta/2)$. Angular distance is measured in units of $\Delta R \equiv \sqrt{(\Delta\eta)^2 + (\Delta\phi)^2}$.

Table 1: Summary of nominal SM background processes considered in the analysis along with a description of the event generators used for matrix element (ME) generation, the set of parton distribution functions (PDF), the hadronisation, parton shower (PS) and underlying event (UE) model, and the underlying event tune.

Process	ME Generator	ME PDF	PS/UE model	UE Tune
SM HH (ggF)	Powheg Box v2	PDF4LHC15nlo	Pythia 8.244	A14
SM HH (VBF)	MadGraph5_aMC@NLO 2.7.3	NNPDF3.0nlo	Pythia 8.244	A14
$t\bar{t}$	Powheg Box v2	NNPDF3.0nlo	Pythia 8.230	A14
single-top	Powheg Box v2	NNPDF3.0nlo	Pythia 8.230	A14
$t\bar{t}+W/Z$	MadGraph5_aMC@NLO 2.3.3	NNPDF3.0nlo	Pythia 8.210	A14
W/Z + jets	Sherpa 2.2.1	NNPDF3.0nnlo	Sherpa 2.2.1	Sherpa default
WW, WZ, ZZ	Sherpa 2.2.1/Sherpa 2.2.2	NNPDF3.0nnlo	Sherpa 2.2.1/Sherpa 2.2.2	Sherpa default
ggF, H	Powheg Box v2	NNPDF3.0nlo	Pythia 8.212	AZNLO
VBF, H	Powheg Box v2	NNPDF3.0nlo	Pythia 8.230	AZNLO
WH, ZH	Powheg Box v2	NNPDF3.0nlo	Pythia 8.230/Pythia 8.186	AZNLO
ttH	Powheg Box v2	NNPDF3.0nlo	Pythia 8.230	A14

3 Data and Monte Carlo samples

The analysis is based on the full Run-2 dataset collected in pp collisions at the LHC with a centre-of-mass energy of $\sqrt{s} = 13$ TeV and a 25 ns bunch crossing interval. The data used in this analysis are required to be recorded while all relevant components of the ATLAS detector were in their nominal operating conditions [31]. The integrated luminosity of the dataset collected over the full Run-2 data-taking period and suitable for physics analysis corresponds to 140 fb^{-1} [32]. The candidate events with oppositely charged leptons are selected based on a combination of single-lepton and di-lepton triggers.[2] The use of a given trigger depends on the flavour and the transverse momenta (p_{T}) of the two leptons in the event, and on the data-taking period. Single-lepton triggers have p_{T} thresholds between 21 GeV and 28 GeV. Di-lepton triggers are only considered if no single-lepton trigger criteria are met and have p_{T} thresholds as low as 13(9) GeV for the leading (sub-leading) lepton.

Monte Carlo (MC) simulation [33] is generally used to model the HH signal and SM background processes. The generation of the physics processes of interest, including the underlying event and immediate decays, are carried out by dedicated event generators. The generated events are then passed through a simulation of the ATLAS detector based on Geant4 [34]. Some background MC event samples, including Z+jets with 10 GeV $< m_{\ell\ell} <$ 40 GeV and the $t\bar{t}$ and Wt alternative samples used for estimating systematic uncertainties, are simulated through the ATLAS fast simulation framework, Atlfast-II (AF2) [33] instead. Additionally, the effect of multiple interactions in the same and neighbouring bunch crossings (pile-up) is modelled by overlaying the simulated hard-scattering event with inelastic pp events generated with Pythia 8.186 [35] using the NNPDF2.3lo set of parton distribution functions (PDF) [36] and the A3 set of tuned parameters [37]. A summary of the event samples used for the simulation of the signal and background processes is shown in Table 1.

SM HH signal events produced via the ggF production mechanism are generated with Powheg Box v2 at next-to-leading order (NLO) interfaced with Pythia 8.244 [38] using the PDF4LHC15nlo [39] PDF set and the A14 tune [40]. The decays of bottom and charm hadrons were performed by EvtGen 1.6.0 [41].

[2] Distinct sets of single-lepton triggers are used for electrons and muons. Di-lepton triggers require either two electrons, two muons, or one electron and one muon.

For parton shower variations, Herwig 7.1.5 [42] is used instead. Samples for non-SM ggF production, i. e. with $\kappa_\lambda \neq 1$ are obtained from simulated samples at different values of these coupling modifiers and combined using morphing techniques [43] with detailed validation studies of this procedure available in Ref. [44]. The SM VBF HH signal samples are generated with MadGraph5_aMC@NLO 2.7.3 [45] using the NNPDF3.0nlo [46] PDF set and the A14 tune [40] interfaced to Pythia 8.244 [38] with Herwig 7.2.1 [42] used for parton shower variations. The decays of bottom and charm hadrons were performed by EvtGen 1.6.0 [41]. As is the case in Ref. [23] signal templates with coupling modifiers ($\kappa_\lambda \neq 1, \kappa_{2V} \neq 1$) are obtained by linear combination of six samples with different values for the κ_λ and κ_{2V} parameters [47]. Therefore five more independent samples with $(0, 0)$, $(1, 0.5)$, $(1, 3)$, $(2, 1)$ and $(10, 1)$ are generated as well with MadGraph interfaced to Pythia8. To vary only κ_{2V} three independent samples are enough: two more independent samples with $\kappa_{2V} = 1.5$ and $\kappa_{2V} = 2$ are generated in the same manner.

SM background processes are generally estimated using simulation, although the cross-sections of the dominant background components, $t\bar{t}$, Wt and Z+jets, are constrained using control regions (CRs) to better predict their contribution in the signal regions (SRs). The estimation is therefore said to be *semi-data-driven* with the normalization being constrained from data and the shape being taken from simulation. For processes not constrained from dedicated CRs, both the shape and the overall normalization are taken from simulation. In addition, the fake-lepton background is estimated in a data-driven way.

SM top-quark production ($t\bar{t}$) and the production of top-quarks in association with W bosons (Wt) contribute as a significant background contamination in the $2b+2\ell+E_{\mathrm{T}}^{\mathrm{miss}}$ final state. At NLO, non-trivial interference arises between these two processes that may be enhanced in phase-space regions with high fractions of Wt events [48]. The two most commonly used schemes to remove the overlap between these two processes are the so-called diagram removal (DR) and diagram subtraction (DS) schemes [49]. The former is used in the present analysis to remove the overlapping events while the latter is used to evaluate the systematic uncertainty in corresponding background event yields.

Production of $t\bar{t}$ events is modelled using the Powheg Box v2 [50–53] generator at NLO with the NNPDF3.0nlo [46] PDF set and the h_{damp} parameter[3] set to 1.5 times the top-quark mass [54]. The events were interfaced to Pythia 8.230 [38] to model the parton shower, hadronisation, and underlying event, with parameters set according to the A14 tune [40] and using the NNPDF2.3lo set of PDFs [36]. The decays of bottom and charm hadrons were performed by EvtGen 1.6.0 [41]. In order to reduce mis-modelling, events are reweighted [55] to match the predictions at NNLO QCD and NLO EW based on the true p_{T}-value of the top-quark (i.e. not the anti-top-quark) provided by the MC event samples.

Production of Wt events is modelled by the Powheg Box v2 [51–53, 56] generator at NLO in QCD using the five-flavour scheme and the NNPDF3.0nlo set of PDFs [46]. The events were interfaced to Pythia 8.230 [38] using the A14 tune [40] and the NNPDF2.3lo set of PDFs [36].

The V+jets samples ($V = W$ or Z) are simulated with Sherpa 2.2.1 [57] interfaced with NNPDF3.0nlo [36] for both the matrix element (ME) calculation and the parton showering (PS) tuning. The merging of different parton multiplicities is achieved through a matching scheme based on the CKKW-L [58, 59] merging technique using a scale parameter of $Q_{cut} = 20$ GeV. The modelling of higher jet multiplicities relies on the parton shower algorithm. The parton shower and underlying event models used are the ones provided internally by Sherpa. The Sherpa 2.2.1 generator adopts a full 5-flavour scheme, with massless b- and $c-$quarks in the matrix elements, while massive quarks can be produced in the parton shower.

[3] The h_{damp} parameter is a re-summation damping factor and one of the parameters that controls the matching of Powheg matrix elements to the parton shower and thus effectively regulates the high-p_{T} radiation against which the $t\bar{t}$ system recoils.

The V+jets samples are split according to the p_{T} of the vector boson and the scalar sum of jet transverse momenta, H_{T}, of the event, introducing a cut at generation level and producing samples for different slices in $\max(H_{\mathrm{T}}, p_{\mathrm{T}}^{V})$ where p_{T}^{V} is defined as the transverse momentum of the true lepton pair from the decay of the V boson. The samples are also generated by applying different filters to select the flavour composition of the jets produced in association with the V boson.

Di-boson processes with four charged leptons, three charged leptons and one neutrino, or two charged leptons and two neutrinos are simulated with the Sherpa 2.2.2 event generator [57] and di-boson processes with leptons and jets are simulated with Sherpa 2.2.1 [57]. Matrix elements contain all diagrams with four electroweak vertices. They are calculated for up to one parton at NLO and up to three partons at LO using Comix [60] and OpenLoops [61], and merged with the Sherpa parton shower according to the ME+PS@NLO prescription [62]. The NNPDF3.0nnlo PDF set is used in conjunction with dedicated parton shower tuning developed by the Sherpa authors. The event generator cross-sections are used in this case (already at NLO).

Finally, single Higgs boson samples from all the main production modes ggF, VBF, Higgs-strahlung (WH, ZH) and associated production with a pair of top (ttH) are considered. For all Higgs boson samples the decays of bottom and charm hadrons were performed by EvtGen 1.6.0 [41] and the normalization accounts for the decay branching ratio calculated with HDECAY [63–65] and Prophecy4f [66–68]. Higgs boson production via gluon–gluon fusion is simulated at NNLO accuracy in QCD using Powheg Box v2 [51–53, 69, 70]. The simulation achieved NNLO accuracy for arbitrary inclusive $gg \rightarrow H$ observables by reweighting the Higgs boson rapidity spectrum in Hj-MiNLO [71–73] to that of HNNLO [74]. The NNPDF3.0nlo [46] PDF set and the AZNLO tune [75] of Pythia 8.212 [38] were used. The gluon–gluon fusion prediction from the MC event samples is normalised to the next-to-next-to-next-to-leading-order cross-section in QCD plus electroweak (EW) corrections at NLO [76–86]. Higgs boson production via vector-boson fusion is simulated with Powheg Box v2 [51–53, 87] and interfaced with Pythia 8.230 [38] for parton shower and non-perturbative effects, with parameters set according to the AZNLO tune [75]. The Powheg Box prediction is accurate to NLO and uses the NNPDF3.0nlo [46] PDF set. It is normalised to an approximate-NNLO QCD cross-section with NLO EW corrections [88–90]. Higgs boson production in association with a vector boson is simulated using Powheg Box v2 [51–53, 87] and interfaced with Pythia 8.230 [38] for parton shower and non-perturbative effects. The Powheg Box prediction is accurate to NLO for VH boson plus one-jet production. The loop-induced $gg \rightarrow ZH$ process is generated separately at leading order. The NNPDF3.0nlo [46] PDF set and the AZNLO tune [75] of Pythia 8.186 [38] were used. The MC prediction is normalised to cross-sections calculated at NNLO in QCD with NLO EW corrections for $q\bar{q}/qg \rightarrow VH$ and at NLO and next-to-leading-logarithm accuracy in QCD for $gg \rightarrow ZH$ [91–97]. The production of ttH events is modelled using the Powheg Box v2 [50–53, 98] generator at NLO with the NNPDF3.0nlo [46] PDF set. The events were interfaced to Pythia 8.230 [38] using the A14 tune [40] and the NNPDF2.3lo [46] PDF set.

4 Object definition and event selection

Proton-proton interaction vertices are reconstructed in events with at least two tracks, each with $p_{\mathrm{T}} > 0.5$ GeV. The primary hard-scatter vertex for each event is defined as the one with the highest value of the sum of squared track transverse momenta [99].

Electron candidates are reconstructed from energy deposits measured in the electromagnetic calorimeter which are matched to ID tracks [100]. They are required to satisfy $|\eta| < 2.47$, excluding the calorimeter

transition region $1.37 < |\eta| < 1.52$, and have a transverse momentum $p_{\mathrm{T}} > 10\,\mathrm{GeV}$. Electron candidates are required to satisfy a 'medium' identification criterion based on the use of shower shape, track–cluster matching and TRT parameters in a likelihood-based algorithm [100]. Additionally, a 'loose' isolation requirement [100] is applied to electron candidates to ensure that they are well separated from other objects in the event. This requirement is based on the momentum of nearby tracks and calorimeter energy deposits within a cone around the electron candidate.

Muon candidates are reconstructed from high-quality tracks found in the MS [101]. A matching of these tracks to ID tracks is required in the region $|\eta| < 2.5$. Muon candidates are required to have $|\eta| < 2.7$ and $p_{\mathrm{T}} > 9\,\mathrm{GeV}$, and to satisfy a 'medium' identification criterion [102]. Additionally, a 'loose' isolation requirement [102] is imposed on muon candidates to ensure that they are well separated from other objects in the event. This requirement is based on investigating the nearby activities within a cone around the muon candidate.

Jets are reconstructed using the anti-k_t algorithm [103, 104] with a radius parameter of $R = 0.4$. It is applied to $|\eta| < 4.5$ noise-suppressed positive-energy topological energy clusters [105, 106] and charged particle tracks processed using a particle-flow algorithm [107]. Pile-up is taken into account in the formation of topological energy clusters [108]. Jet candidates are required to have $p_{\mathrm{T}} > 20\,\mathrm{GeV}$ and those with $|\eta| < 2.5$ are considered to select the candidate jets for the reconstruction of the hadronic decay of the Higgs to b-tagged jets while jets with $|\eta| > 2.5$ are considered 'forward' jets. To reject jet candidates originating from pile-up interactions, they must satisfy a tight pile-up suppression requirement based on a multivariate method [109]. The method removes jets that appear inconsistent with the primary vertex and have $p_{\mathrm{T}} < 60\,\mathrm{GeV}$ [99]. In the end, a neural network-based b-tagging algorithm [110] is used to identify jets containing b-hadrons (b-tagged jets) at a 77% efficiency working point in simulated $t\bar{t}$ events. The rejection rate for this working point is ∼6 for jets originating from c-quarks and ∼200 for jets originating from light quarks [110].

The missing transverse momentum, $\boldsymbol{p}_{\mathrm{T}}^{\mathrm{miss}}$, the magnitude of which is denoted as $E_{\mathrm{T}}^{\mathrm{miss}}$, quantifies the amount of energy and momentum carried by invisible particles that do not interact with the detector. It is determined as the magnitude of the negative vectorial sum of the transverse momenta of the selected and calibrated physics objects, including jets, electrons, and muons, and inner detector tracks from the hard-scatter collision vertex not associated with any physics object [111].

Different reconstructed objects can share the same detector signature, leading to ambiguities in the identification of these objects. To resolve these ambiguities, as in [22], an overlap removal procedure is performed sequentially, such that only objects that survive the previous step are considered in the following steps. The steps are as follows: if any electrons share a track, only the highest p_{T} electron is kept. If a hadronically decaying τ-lepton candidate is within $\Delta R_y = 0.2$[4] of any electron or muon, it is removed. If an electron and a muon share a track the muon is kept only if it is associated with a signature in the muon spectrometer. Any jet within $\Delta R_y = 0.2$ of an electron and subsequentially any electron within $\Delta R_y = 0.4$ of any jet is removed. Any jet within $\Delta R_y = 0.2$ of a muon or having an inner detector track ghost-matched [112] to a muon within $\Delta R_y = 0.2$ of the jet, is removed if it has fewer then three associated tracks. Any muon within $\Delta R_y = 0.4$ of a jet is removed as well as any jet within $\Delta R_y = 0.2$ of a hadronically decaying τ-lepton candidate.

The analysis selects candidate events that contain exactly two opposite-charge light leptons, either electrons or muons, and exactly two $b-$tagged jets. While the signal processes contain sources of $E_{\mathrm{T}}^{\mathrm{miss}}$ an explicit

[4] This is the angular distance ΔR considering the rapidity y instead of the pseudorapidity η.

Table 2: Cutflow for event selection using SM $gg/qq \to HH$ signal samples in various decay channels. For both ggF and VBF signal samples, the SM HH cross-section, σ, and branching ratio, $\mathcal{B}$, are assumed when computing event yields for a luminosity of $\mathcal{L} = 140\,\text{fb}^{-1}$. Efficiencies are different for $bbZZ(\to 2\ell 2\nu)$ compared to $bbZZ(\to 2\ell 2q)$ since the initial number of events considers $Z \to \tau\tau$ while the former does not.

ggF and VBF event selection cut	$bbWW$		$bb\tau\tau$		$bbZZ(\to 2\ell 2\nu)$		$bbZZ(\to 2\ell 2q)$	
	ggF	VBF	ggF	VBF	ggF	VBF	ggF	VBF
Initial number of events ($\mathcal{L} \times \sigma \times \mathcal{B}$)	70	3.9	39	2.2	3.8	0.21	18	1.0
$N_{\text{leptons}} = 2$, opposite sign, pass trigger requirement	22	0.99	8.3	0.35	1.3	0.057	3.6	0.17
$N_{b\text{-jets}} = 2$	9.8	0.39	3.7	0.14	0.57	0.022	1.6	0.067

selection on $E_{\text{T}}^{\text{miss}}$ is not performed to ensure high training statistics available for the MVA discriminants. To suppress the contribution of misidentified jets, the analysis excludes events that contain jets satisfying one of the bad jet criteria [109]. The yields of the ggF and VBF signal samples at different preselection steps are summarized in Table 2, about an order of magnitude of reduction in the event yields is observed from this initial selection.

The events that satisfy the preselection criteria are further divided into two categories: the signal region (SR) and dedicated background control regions (CRs) for Z plus heavy flavour jets (Z+HF), $t\bar{t}$ and Wt, as depicted in Figure 3. The greyed out region is not considered since it does not add significantly to the sensitivity. The CRs are used to constrain the background normalization in the SRs. The SR and CRs are separated based on the invariant mass of the two leptons, with a lower threshold set at 15 GeV and an upper threshold set at 75 GeV for same flavour (SF) leptons and 110 GeV for different flavour (DF) leptons, as illustrated in Figure 3(a) and Figure 3(b). The mass of the di-lepton system is required to be $m_{\ell\ell} > 110\,\text{GeV}$ for the CRs enriched in events coming from top-quark processes. This region is further split into dedicated $t\bar{t}$- and Wt-enriched control regions by requiring $m_{b\ell}$ [48][5] to be below or above 250 GeV, respectively. The Z+HF CR is required to have two SF leptons in the events, and to satisfy the di-lepton invariant mass requirement, $75\,\text{GeV} < m_{\ell\ell} < 110\,\text{GeV}$, excluding events where the invariant mass of the two b-tagged jets satisfies $40\,\text{GeV} < m_{bb} < 210\,\text{GeV}$. A VBF selection is applied to further categorize the events into two orthogonal ggF/VBF enriched regions by reverting (for ggF-like regions) or applying (for VBF-like regions) the VBF selection. The VBF selection requires the presence of at least two forward jets: these jets must have $p_{\text{T}} > 30\,\text{GeV}$, a maximum pseudorapidity separation between the extra jets larger than 4, and a maximum mass of a pair of two jets larger than 600 GeV. The jets pairs considered are not required to be the same for the pseudorapidity separation and mass requirements; in less than $\sim 1\%$ of the MC events, different pairs of jets are chosen. The VBF selection has a relative selection efficiency of $\sim 60\%$ on VBF signal events. Table 3 shows the yields for SM background processes and non-resonant SM ggF and VBF signals in the SRs and CRs. The SRs are then used to extract the final results, with the backgrounds constrained by the CRs, as described later. To enhance the sensitivity to the signal process and maximize the rejection of the expected SM backgrounds, a multivariate approach is used to select signal events, as described in the next section.

[5] See Table 4 for its definition.

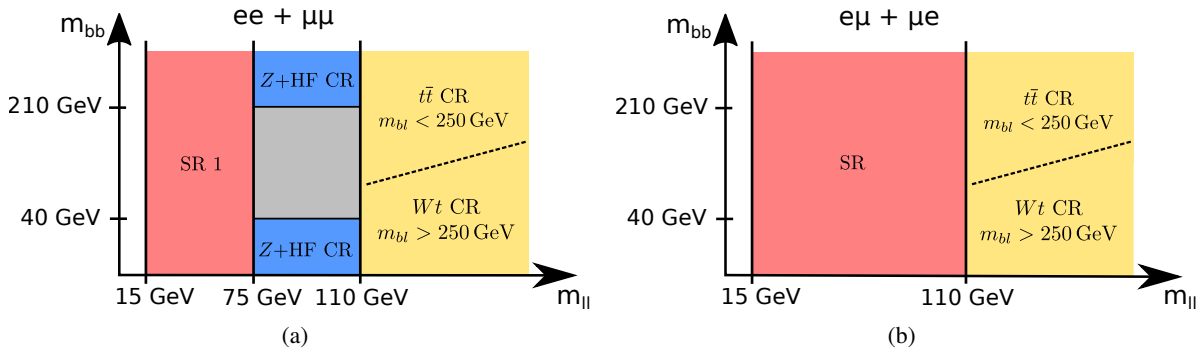

Figure 3: Definition of signal and control regions for same lepton flavour (a) and different lepton flavour (b) events. The greyed-out region is excluded as it has a negligible contribution to the final results. The $m_{b\ell}$ discriminant variable [48] is used to further separate the top CR into separate $t\bar{t}$ and Wt control regions.

Table 3: Pre-fit yields for SM background processes and non-resonant SM ggF and VBF signals in the SRs and CRs. The event yields in the row 'Fakes' come from the data-driven fake-lepton background estimation described in Section 6. The event yields for Z+jets processes are split into ones with heavy-flavour (HF) and light-flavour (LF) jets as defined in Section 6. A dash represents no contribution of the respective MC event sample in the respective region. Uncertainties are from MC statistics and template statistics only.

Process	**ggF-SR**	**VBF-SR**	**$t\bar{t}$-CR**	**Wt-CR**	**Z+HF-CR**
SM background					
$t\bar{t}$	561220 ± 150	52670 ± 50	436840 ± 130	2270 ± 10	34700 ± 40
$t\bar{t}+V$	1121 ± 4	194.7 ± 1.9	1133 ± 5	97.0 ± 1.1	440.1 ± 1.9
Single top (Wt)	16260 ± 50	1165 ± 12	14100 ± 40	2901 ± 20	1237 ± 13
Single top (s/t-channel)	12.7 ± 0.8	2.48 ± 0.35	1.21 ± 0.28	0.35 ± 0.14	0.25 ± 0.11
$Z \to \ell\ell$ (HF)	16090 ± 180	1178 ± 34	3610 ± 70	525 ± 11	43390 ± 260
$Z \to \ell\ell$ (LF)	2720 ± 170	260 ± 40	600 ± 90	55 ± 8	5470 ± 190
$Z \to \tau\tau$ (HF)	2200 ± 40	154 ± 13	3 ± 7	1.9 ± 0.5	4 ± 6
$Z \to \tau\tau$ (LF)	370 ± 50	24 ± 4	-1.3 ± 1.5	0.11 ± 0.06	0.8 ± 0.5
W+jets	0.7 ± 0.5	0.09 ± 0.08	-0.2 ± 0.4	—	—
Diboson	288 ± 4	32.6 ± 0.8	159.0 ± 2.8	39.0 ± 0.9	226.8 ± 3.3
Single Higgs	601.0 ± 1.1	105.1 ± 0.4	336.5 ± 0.5	22.06 ± 0.12	48.28 ± 0.29
Fakes	18510 ± 170	2390 ± 60	10020 ± 140	529 ± 35	1360 ± 50
Total SM bkg.	619390 ± 350	58170 ± 100	466810 ± 230	6440 ± 40	86890 ± 330
HH signal, ggF					
ggF $HH \to bbWW$	8.318 ± 0.016	0.857 ± 0.005	0.00113 ± 0.00019	0.00033 ± 0.00010	0.0014 ± 0.0002
ggF $HH \to bb\tau\tau$	3.138 ± 0.009	0.3284 ± 0.0029	0.00332 ± 0.00029	0.00068 ± 0.00015	0.0047 ± 0.0004
ggF $HH \to bbZZ$	0.633 ± 0.005	0.0873 ± 0.0018	0.00083 ± 0.00018	0.00020 ± 0.00009	0.0442 ± 0.0013
$\sum$ ggF HH	12.088 ± 0.019	1.272 ± 0.006	0.0053 ± 0.0004	0.00121 ± 0.00020	0.0504 ± 0.0014
HH signal, VBF					
VBF $HH \to bbWW$	0.1518 ± 0.0014	0.2138 ± 0.0017	0.00013 ± 0.00004	—	0.00009 ± 0.00004
VBF $HH \to bb\tau\tau$	0.0537 ± 0.0006	0.0769 ± 0.0007	0.000086 ± 0.000022	0.000048 ± 0.000018	0.00024 ± 0.00004
VBF $HH \to bbZZ$	0.0097 ± 0.0004	0.0184 ± 0.0006	0.000040 ± 0.000024	0.0000029 ± 0.0000016	0.00236 ± 0.00023
$\sum$ VBF HH	0.2152 ± 0.0016	0.3091 ± 0.0019	0.00026 ± 0.00005	0.000051 ± 0.000018	0.00269 ± 0.00024
HH signal, ggF+VBF					
$\sum$ ggF+VBF HH	12.303 ± 0.019	1.582 ± 0.006	0.0055 ± 0.0004	0.00126 ± 0.00020	0.0531 ± 0.0014

5 Multivariate analyses

Events that pass the selections described in previous section are then passed through a MVA to separate rare signal events from the large amount of background events. A DNN and a Boosted Decision Tree (BDT) are used to classify events in ggF and VBF categories, respectively. The output of the MVA models are used as discriminants in the statistical analysis discussed in Section 8.

In the ggF category, the Keras library [113] with Tensorflow as backend [114] is used to design a DNN classifier with a multi-output architecture to optimise the separation between ggF HH signal, background from $t\bar{t}$ and Wt and all other background processes simultaneously. In a first stage, 50% of the simulated events are used to optimize the set of input variables and the hyperparameters of the DNN in a five-fold cross-validation with a train/test split fraction of 80%/20%. The final set of input variables is selected based on the permutation feature importance [115] to keep only the most important ones; this strategy allows to not compromise the performance but reduces the complexity of the model and therefore its goodness given the finite training statistics. These input variables are listed in Table 4, with $E_{\mathrm{T}}^{\mathrm{miss}}$ significance being ranked as ninth and $E_{\mathrm{T}}^{\mathrm{miss}}$ being ranked as the twelfth most important input variable with respect to the overall sensitivity. It has been checked that data is well described by MC for these variables. The hyperparameters of the DNN are optimized through an automatic process using the Optuna [116] package, with the figure of merit being the 95% CL upper limit on the signal strength, i. e. the ratio of the measured HH production cross section to its SM prediction, without considering systematic uncertainties, using the CL_s prescription [117]. The final DNN model includes nine fully connected (FC) layers, each with 512 nodes, and is trained at a learning rate of 0.00011, with ReLU activations [118] used for the FC layers and softmax activations used for the output layer. It is trained with a two-fold cross-validation strategy with a train/test split fraction of 50%/50%. A dropout rate of 0.3 is applied to the FC layers to prevent over-fitting, as a result the loss curve reaches a plateau for both training and test datasets at the end of the training. The score of the signal output node is binned so that the statistical uncertainty of the backgrounds is less than 30% and ~ 1 HH signal event from the combined ggF and VBF production modes is expected in each bin. The seven bins with highest DNN output score are further considered for the statistical analysis, leading to a maximum of $O(10^2)$ background events being present in a bin to be considered as part of the final signal region.

In contrast to the ggF event category, due to limited statistics and a tighter phase space in the VBF category, a DNN approach cannot be fully exploited for such events. Therefore, a BDT classifier is trained using the adaptive boosting (`AdaBoost`) method and the TMVA framework [122] with a cross-validation setup. Input variables are listed in Table 5, with $E_{\mathrm{T}}^{\mathrm{miss}}$ significance being ranked as the fourteenth most important input variable with respect to the overall sensitivity. It has been checked that data is well described by MC for these variables. The training parameters are optimized to have 350 trees with a maximum depth of four and a minimum terminal node size of 2.5%. The signal tree provided to the algorithm consists exclusively of VBF HH events, while the background consists of ggF HH signal events and other SM background events. ggF HH events are classified as background since maximising the sensitivity to the VBF HH production mode is the goal of this MVA discriminant. A two-fold cross-validation was utilized with a train/test split fraction of 50%/50%. Each BDT was employed for the half of the dataset it had not been trained on, ensuring a reliable evaluation of performance across the entire dataset. After careful examination, it has been decided to train the BDT on a VBF sample with $\kappa_\lambda = 0$, as it showed the best overall performance across a set of SM and BSM scenarios. The BDT output score is binned into ten bins taking into account their signal over background ratio with the most sensitive bin being required to have a minimum of ~ 2 background events. The five bins with highest BDT output score are further considered

Table 4: Input features used for the DNN in the ggF category. Indices 0 and 1 refer to p_{T}-leading and p_{T}-sub-leading objects respectively.

Input feature	Description
same flavour	Unity if final state leptons are ee or $\mu\mu$, zero otherwise
p_{T}^{ℓ}, p_{T}^{b}	transverse momenta of the leptons, b-tagged jets
$m_{\ell\ell}$, $p_{\mathrm{T}}^{\ell\ell}$	invariant mass and the transverse momentum of the di-lepton system
m_{bb}, p_{T}^{bb}	invariant mass and the transverse momentum of the b-tagged jet pair system
m_{T2}^{bb}	stransverse mass of the two b-tagged jets [119, 120]
$\Delta R_{\ell\ell}$, ΔR_{bb}	ΔR between the two leptons and two b-tagged jets
$m_{b\ell}$	$\min\{\max(m_{b_0\ell_0}, m_{b_1\ell_1}), \max(m_{b_0\ell_1}, m_{b_1\ell_0})\}$ [48]
$\min \Delta R_{b\ell}$	minimum ΔR of all b-tagged jet and lepton combinations
$m_{bb\ell\ell}$	invariant mass of the $bb\ell\ell$ system
$E_{\mathrm{T}}^{\mathrm{miss}}$, $E_{\mathrm{T}}^{\mathrm{miss}}$-sig	missing transverse energy and its significance [121]
$m_{\mathrm{T}}(\ell_0, E_{\mathrm{T}}^{\mathrm{miss}})$	transverse mass of the p_{T}-leading lepton w.r.t. to $E_{\mathrm{T}}^{\mathrm{miss}}$
$\min m_{\mathrm{T},\ell}$	minimum value of $m_{\mathrm{T}}(\ell_0, E_{\mathrm{T}}^{\mathrm{miss}})$ and $m_{\mathrm{T}}(\ell_1, E_{\mathrm{T}}^{\mathrm{miss}})$
$H_{\mathrm{T2}}^{\mathrm{R}}$	measure for boostedness of the two Higgs bosons, see definition in footnote[6]

for the statistical analysis, leading to a maximum of $O(10^3)$ background events being present in a bin to be considered as part of the final signal region.

6 Background estimation

The dominant background processes expected to contribute to the signal region are top quark pair production ($t\bar{t}$), single top-quark in association with a W boson (Wt), and Z/γ^* production in association with heavy-flavour jets. The contributions of these background processes are constrained in dedicated CRs as defined in Section 4.

The simulated Z+jets background events are divided into heavy flavour (HF) and light flavour (LF) based on the generator-level information on the true origin of the jets. If at least one of the two p_{T}-ordered leading jets in the Z+jets sample is matched at generator level with either a b- or c-quark, events are classified as 'heavy flavour'. All other Z+jets events, i. e. events where at least one of the two p_{T}-leading jets is a light flavour jet, are classified as light flavour. As the cross-section of Z boson production in association with heavy flavour jets is known to be mis-modelled [125, 126], the MC prediction is constrained with data in control regions enriched in the Z+HF processes.

The contribution from events containing photons or jets which are mis-identified as leptons as well as leptons from the hadronic decays of heavy flavour quarks is collectively referred as 'fake-lepton' background. It is estimated using a data-driven method.

Firstly, the corresponding CR is defined to have the same selections as the SR, except reverting the opposite-sign (OS) requirement of the di-lepton system in the SR definition to have only same-sign (SS) lepton pairs. The contribution of fake-lepton events in the SS region is then estimated by subtracting

[6] $H_{\mathrm{T2}}^{\mathrm{R}} = \dfrac{\left|\boldsymbol{E}_{\mathrm{T}}^{\mathrm{miss}} + \boldsymbol{p}_{\mathrm{T}}^{\ell_0} + \boldsymbol{p}_{\mathrm{T}}^{\ell_1}\right| + \left|\boldsymbol{p}_{\mathrm{T}}^{b_0} + \boldsymbol{p}_{\mathrm{T}}^{b_1}\right|}{\left|\boldsymbol{E}_{\mathrm{T}}^{\mathrm{miss}}\right| + \left|\boldsymbol{p}_{\mathrm{T}}^{\ell_0}\right| + \left|\boldsymbol{p}_{\mathrm{T}}^{\ell_1}\right| + \left|\boldsymbol{p}_{\mathrm{T}}^{b_0}\right| + \left|\boldsymbol{p}_{\mathrm{T}}^{b_1}\right|}$

Table 5: Input features for the BDT algorithm in the VBF category. The usage of j in variable names refers to only non b-tagged jets being considered. Indices 0 and 1 refer to p_{T}-leading and p_{T}-sub-leading objects respectively.

Input feature	Description
η_{ℓ_0} , η_{ℓ_1}, ϕ_{ℓ_0}, ϕ_{ℓ_1}, $p_{\mathrm{T}}^{\ell_0}$, $p_{\mathrm{T}}^{\ell_1}$	η, ϕ, p_{T} of the p_{T}-(sub)leading lepton
η_{b_0}, η_{b_1}, ϕ_{b_0}, ϕ_{b_1}, $p_{\mathrm{T}}^{b_0}$, $p_{\mathrm{T}}^{b_1}$	η, ϕ, p_{T} of the p_{T}-(sub)leading b-tagged jet
η_{j_0}, η_{j_1}, ϕ_{j_0}, ϕ_{j_1}, $p_{\mathrm{T}}^{j_0}$, $p_{\mathrm{T}}^{j_1}$	ϕ, η, p_{T} of the p_{T}-(sub)leading non b-tagged jet
$E_{\mathrm{T}}^{\mathrm{miss}}$, $\phi^{E_{\mathrm{T}}^{\mathrm{miss}}}$, $E_{\mathrm{T}}^{\mathrm{miss}}$-sig	missing transverse energy, its ϕ and significance [121]
p_{T}^{bb}, ΔR_{bb}, $\Delta\phi_{bb}$, m_{bb}	p_{T}, ΔR, $\Delta\phi$ and invariant mass of di-b-jet system
$p_{\mathrm{T}}^{\ell\ell}$, $\Delta R_{\ell\ell}$, $\Delta\phi_{\ell\ell}$, $m_{\ell\ell}$, $\phi^{\ell\ell}_{\mathrm{centrality}}$	p_{T}, ΔR, $\Delta\phi$, p_{T} and centrality of di-leptons system
$p_{\mathrm{T}}^{bb\ell\ell}$, $m_{bb\ell\ell}$	p_{T} and invariant mass of the $bb\ell\ell$ system
$p_{\mathrm{T}}^{bb\ell\ell+E_{\mathrm{T}}^{\mathrm{miss}}}$, $m_{bb\ell\ell+E_{\mathrm{T}}^{\mathrm{miss}}}$	p_{T} and invariant mass of $bb\ell\ell + E_{\mathrm{T}}^{\mathrm{miss}}$ system
$m_{\ell\ell+E_{\mathrm{T}}^{\mathrm{miss}}}$	invariant mass of di-lepton + $E_{\mathrm{T}}^{\mathrm{miss}}$ system
$p_{\mathrm{T}}^{E_{\mathrm{T}}^{\mathrm{miss}}+\ell\ell}$, $\Delta\phi_{E_{\mathrm{T}}^{\mathrm{miss}},\ell\ell}$	p_{T} of and $\Delta\phi$ between $E_{\mathrm{T}}^{\mathrm{miss}}$ and di-lepton system
$p_{\mathrm{T}}^{\mathrm{tot}}$	p_{T} of $bb\ell\ell + E_{\mathrm{T}}^{\mathrm{miss}}$+ p_{T}-leading and -sub-leading jet
m_{tot}	invariant mass of $bb\ell\ell + E_{\mathrm{T}}^{\mathrm{miss}}$+ p_{T}-leading and -sub-leading jet
m_t^{KLF}	Kalman fitter top-quark mass [123]
$\min \Delta R_{\ell_0 j}$, $\min \Delta R_{\ell_1 j}$	minimum ΔR between p_{T}-(sub)leading ℓ-j couples
$\sum m_{\ell j}$	sum of the invariant masses of all ℓ+jet combinations
$\max p_{\mathrm{T}}^{jj}$, $\max m_{jj}$	maximum p_{T} and invariant mass of any two non b-tagged jets
$\max \Delta\eta_{jj}$, $\max \Delta\phi_{jj}$	maximum $\Delta\eta$ and $\Delta\phi$ between any two non b-tagged jets
$\min \Delta R_{b\ell}$	minimum ΔR of all b-tagged jet and lepton combinations
$N_{\text{forward jets}}$, N_j	number of forward jets, number of non b-tagged jets
m_{T2}^{bb}	stransverse mass of the two b-tagged jets [119, 120]
m_{coll}	collinear mass (reconstruction of $m_{\tau\tau}$) [124]
m_{MMC}	value of the MMC algorithm (reconstruction of $m_{\tau\tau}$) [124]

the predicted contribution from prompt leptons of SM backgrounds from the observed number of the SS di-lepton events in data. Next, transfer factors binned as function of sub-leading lepton p_{T} are calculated as the ratio of the number of OS fake-lepton events to the number of SS fake-lepton events

$$f_{\mathrm{SS}\to\mathrm{OS}} = \frac{N_{\mathrm{MC,OS}}^{\mathrm{fake}}}{N_{\mathrm{MC,SS}}^{\mathrm{fake}}}$$

as estimated from the background MC events and range from 1.2 to 1.9. In the end, the number of the fake-lepton events in the SRs is extrapolated by applying the transfer factors to the number of fake-lepton events estimated in the SS region:

$$N_{\mathrm{OS}}^{\mathrm{fake}} = f_{\mathrm{SS}\to\mathrm{OS}} \times \left(N_{\mathrm{data,SS}} - N_{\mathrm{MC,SS}}^{\mathrm{prompt}}\right).$$

7 Systematic uncertainties

The results account for several sources of systematic uncertainty for the signal and background processes, which are classified as either experimental (detector or luminosity related) or theoretical modelling

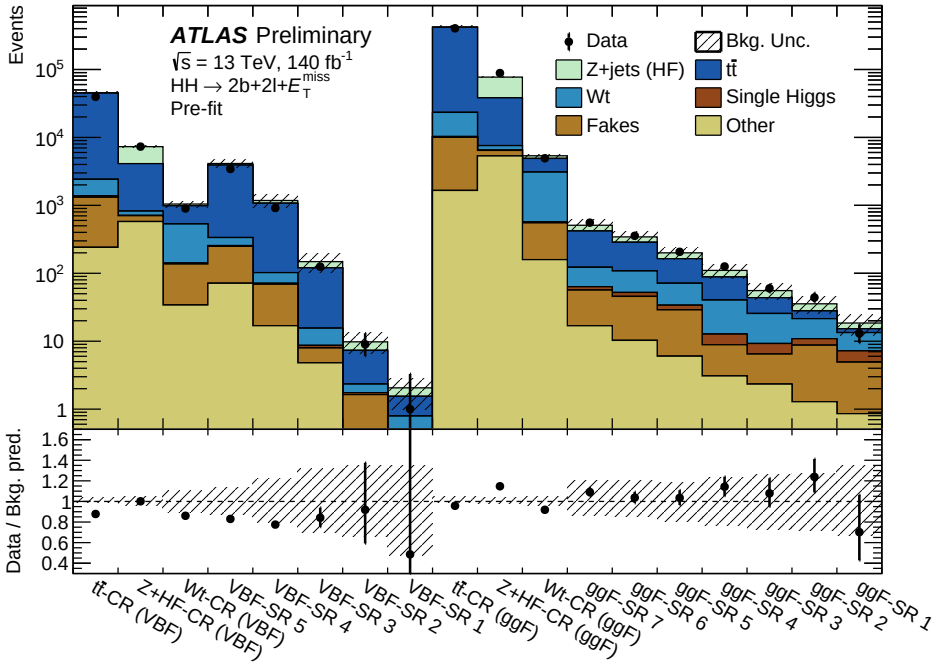

Figure 4: Pre-fit yields of $t\bar{t}$, Z+HF and Wt CRs, both for the ggF and VBF event selection, as well as the highest-score bins, numbered from high (VBF-SR 1 and ggF-SR 1) to low score (VBF-SR 5 and ggF-SR 7), of the BDT and DNN output distribution in the VBF and ggF event categories, respectively, as used in the final result. The shaded bands include both statistical and systematic uncertainties.

uncertainties. Statistical uncertainties of the simulated event samples are also taken into account. The total pre-fit event yields, with their uncertainties, and the background composition in the different signal and control regions are shown in Figure 4.

The uncertainties due to experimental sources are primarily due the mismeasurement of reconstructed object momentum and from the finite level of precision when determining reconstruction efficiencies. They include uncertainties of the jet energy scale [108] and jet energy resolution [127]. Additional uncertainties for b-tagged jets arise from the precision of the b-tagging efficiency and from the rates at which charm- and light-flavoured jets are selected as b-tagged jets [110]. Lepton-related uncertainties arise of the electron [100] and muon [105] reconstructed energy (momentum) measurements, as well as from the precision of their reconstruction and identification efficiencies. The $E_{\mathrm{T}}^{\mathrm{miss}}$ scale and resolution [111] uncertainties, as well as uncertainties from the mis-modelling of pile-up, trigger efficiency and luminosity, are also taken into account. The uncertainty in the combined 2015–2018 integrated luminosity is 0.83% [32], obtained using the LUCID-2 detector [128] for the primary luminosity measurements, complemented by measurements using the inner detector and calorimeters.

The normalization corrections of the dominant background processes, namely $t\bar{t}$, Wt and Z + jets, are determined using data in the control regions during the statistical analysis. The experimental uncertainties and the systematic uncertainties from the modelling of these processes are taken into account and constrained during the fitting process. For the $t\bar{t}$ and Wt processes, the QCD uncertainty is estimated by comparing events with different renormalization scale (μ_R) and factorization scale (μ_F) settings, where the largest deviation is chosen as the systematic uncertainty. The uncertainties arising from the modelling of initial- and final-state radiation in the generators used to simulate the $t\bar{t}$ (Wt) background processes are evaluated

using the method described in Ref. [129]. The effects of uncertainties due to the choice of PDF and the value of α_S are evaluated by varying the PDF as well as the value for α_S and taking the maximum variation as uncertainty into account. The ME and PS uncertainties are estimated by comparing events from the nominal simulation samples with events from samples using alternative ME generators and PS generators, taking their difference as the respective uncertainty and then symmetrising it. The uncertainty arising from the interference between the NLO predictions for $t\bar{t}$ and Wt processes is estimated by taking the difference between the predicted yields obtained with the DR and DS schemes [129]. The Z + jets modelling uncertainties are estimated using the nominal Sherpa 2.2.1 samples by considering different merging and re-summation scales [130, 131]. The uncertainties due to PDF variations and changes in μ_R and μ_F are calculated using the same procedures as for the $t\bar{t}$ and Wt backgrounds.

Systematic uncertainties in the signal acceptance due to varying μ_R and μ_F, as well as PDF-induced uncertainties, are taken into account as recommended by the LHCXSWG [15] and evaluated using the same procedure as for the top-quark background processes. The uncertainty due to the parton shower modelling is computed by comparing Herwig 7 with Pythia 8. The uncertainty in the HH production cross-section, evaluated to be ±3% for PDF+α_S and $^{+6\%}_{-23\%}$ for the combined scale and top-quark mass scheme for ggF, and ±2.1% for PDF+α_S and $^{+0.03\%}_{-0.04\%}$ for the scale for VBF, is included as an uncertainty in $\sigma^{SM}_{gg/qq\to HH/HHjj}$ when computing the upper limits on the signal strength.

8 Statistical treatment and results

8.1 Statistical procedure

The statistical procedure used to interpret the data is described in Ref. [132]. The likelihood function is constructed from the product of Poisson probabilities:

$$L(\text{data}|\,\mu,\theta) = \prod_{i=1}^{N} \text{Poisson}(\text{data}_i|\,\mu\cdot s_i(\theta) + \mu_b b_i(\theta)) \times \text{G}(\tilde{\theta}|\theta)$$

where s_i and b_i are the signal and background contributions in the i-th bin of the fitted variable distribution; μ is the signal strength, μ_b is the normalization factor for the respective background, and θ denotes the nuisance parameters, which account for the uncertainties of the measurements; $\text{G}(\tilde{\theta}|\theta)$ is the Gaussian scaling function of the nuisance parameters constructed as deviations from the nominal model of the systematic uncertainties, where $\tilde{\theta}$ provides a maximum likelihood estimate for θ. The parameter of interest in the statistical analysis is the global signal strength factor $\mu = \sigma/\sigma^{\text{SM}}$, which acts on the total number of events predicted by the signal model. This factor is defined such that $\mu = 0$ corresponds to the background-only hypothesis and $\mu > 0$ corresponds to a HH signal in addition to the background. Hypothesised values of μ are tested based on the profile likelihood ratio [133], which compares data with background-only (b) and signal+background ($s + b$) models using the following test statistic:

$$q_\mu = \begin{cases} -2\ln\frac{L(\text{data}|\,\mu,\hat{\hat{\theta}}_\mu)}{L(\text{data}|\,\hat{\mu},\hat{\theta})} & \hat{\mu} \le \mu \\ 0 & \hat{\mu} > \mu \end{cases}$$

where $\hat{\mu}$ and $\hat{\theta}$ are the values for μ and θ when maximizing L with all parameters floating, which are referred to as the unconditional maximum-likelihood (ML) estimators; $\hat{\hat{\theta}}_\mu$ is the conditional ML estimator

of θ for a fixed value of μ. This test statistic extracts the information on the signal strength from a full likelihood fit to the data. The likelihood function includes all the parameters that describe the systematic uncertainties and their correlations. The constraints on the coupling modifiers are obtained by using the respective modifier (κ_λ or κ_{2V}) in-place of the signal strength as the parameter of interest in the profile likelihood ratio.

Exclusion limits at 95% CL are based on the CL_s prescription [117], and they are set on the HH production cross-section times branching fraction divided by the corresponding SM prediction. The statistical analysis uses the distributions of the MVA output score in both the ggF and VBF SRs as final discriminant. The background CRs are used to constrain the overall normalization for the $t\bar{t}$, Wt and Z+HF backgrounds in the SR. Other background normalizations and shapes are fixed with prior uncertainties included in the fit.

8.2 Limits on HH production

All regions used for this search are displayed in Figure 5 after a fit with the signal strength fixed to the upper limit while pre-fit distributions are shown in Figure 4. A downward fluctuation of the data in the last bin of the both the NN and BDT distributions is observed. A negative signal strength has been extracted from the fit: $\mu_{HH} = -8.5^{+7.7}_{-8.4}$. Using the approach described in Section 8.1, the upper limits on the signal strength parameter for Higgs boson pair production with consideration of both ggF and VBF signals are determined. Figure 6 summarizes ggF, VBF and combined results with the impact of all systematic uncertainties being shown. The observed combined upper limit at 95% CL on the signal strength is $\mu_{HH} = 9.6$. In the CRs, the normalization and modelling of the backgrounds play a prominent role, and they dominate the sources of uncertainty. In the SRs, the systematic uncertainties mostly arise from background modelling, experimental sources and the signal normalization. In the most sensitive bins, i. e. ggF-SR 1 to ggF-SR 3 and VBF-SR 1 and VBF-SR 2, the statistical uncertainty becomes dominant due to the limited number of expected events.

8.3 Constraint on Higgs coupling parameters

This analysis is extended by performing likelihood scans on the κ_λ and κ_{2V} parameters. The single Higgs boson background has a small dependence upon κ_λ through loop effects, which is neglected. Coupling modifiers other than the one tested in the respective scan are set to their SM value. Hence, the κ_t, κ_V and κ_{2V} coupling modifiers are set to $\kappa_t = \kappa_V = \kappa_{2V} = 1$ for the κ_λ-scan. Both the ggF and VBF HH signal regions are used in the analysis, and the result is shown in Figure 7(a). The observed result constrains κ_λ to be within the range $[-6.2, 13.3]$ at 95% CL which is slightly better than the expected range of $[-8.1, 15.5]$ at 95% CL due to the observed underfluctuation of the data.

A scan over the κ_{2V} parameter is also conducted. Again, all other couplings are set to their respective SM value. Although only the VBF production mode of Higgs boson pairs is sensitive to the κ_{2V} coupling modifier, both the ggF and VBF SRs are included in the scan, allowing to achieve a slight enhancement of the sensitivity from the presence of VBF HH events within the ggF SR. A likelihood scan is performed to set constraints on the κ_{2V} parameter, this is shown in Figure 7(b). Values for κ_{2V} are constraint to be within the range of $[-0.17, 2.4]$ at 95% CL which is slightly better than the expected range of $[-0.51, 2.7]$ at 95% CL due to the observed underfluctuation of the data.

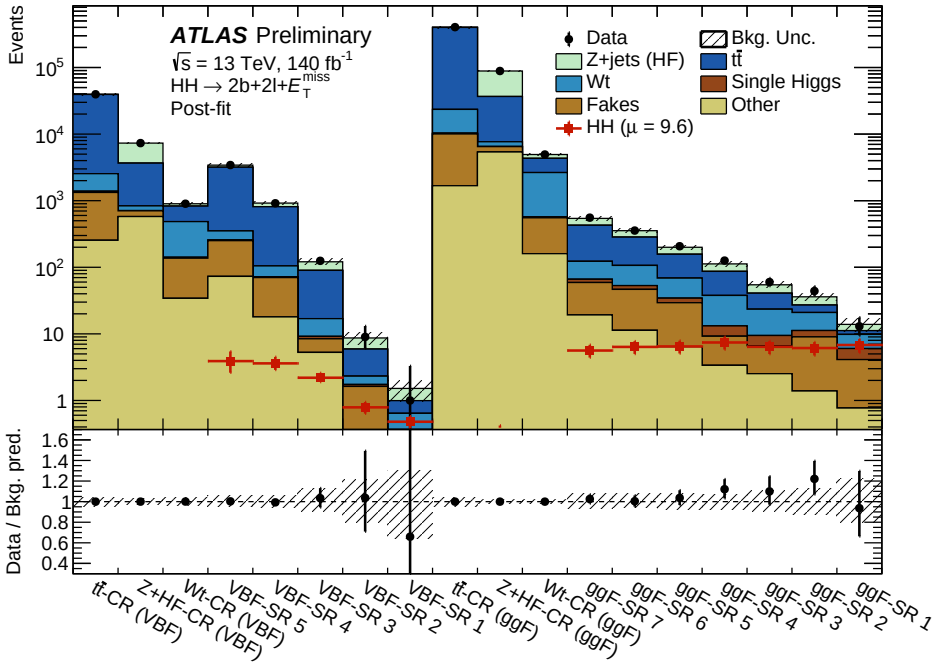

Figure 5: Post-fit yields from the signal+background fit of $t\bar{t}$, Z+HF and Wt CRs, both for the ggF and VBF event selections, as well as the highest-score bins, numbered from high (VBF-SR 1 and ggF-SR 1) to low score (VBF-SR 5 and ggF-SR 7), of the BDT and DNN output distribution in the VBF and ggF event categories respectively as used in the final result. The fit is a conditional fit with the signal strength being fixed to the observed upper limit of $\mu_{HH} = 9.6$. The shaded bands include both statistical and systematic uncertainties.

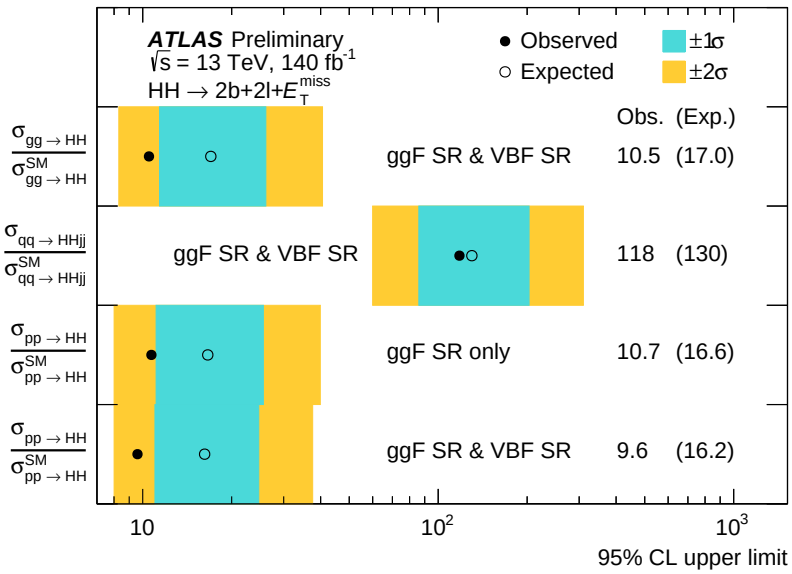

Figure 6: Observed and expected upper limits on the ratios of the Higgs boson pair production cross-section to the corresponding Standard Model prediction $\sigma_{HH}/\sigma_{HH}^{\mathrm{SM}}$ for ggF HH signal only (top row), VBF HH signal only while considering ggF HH as background (second row) and the combined ggF+VBF HH signal considering only the ggF SR (third row) and considering all SRs (bottom row) at a 95% confidence level. The relative ratio between ggF and VBF production modes is fixed to the SM.

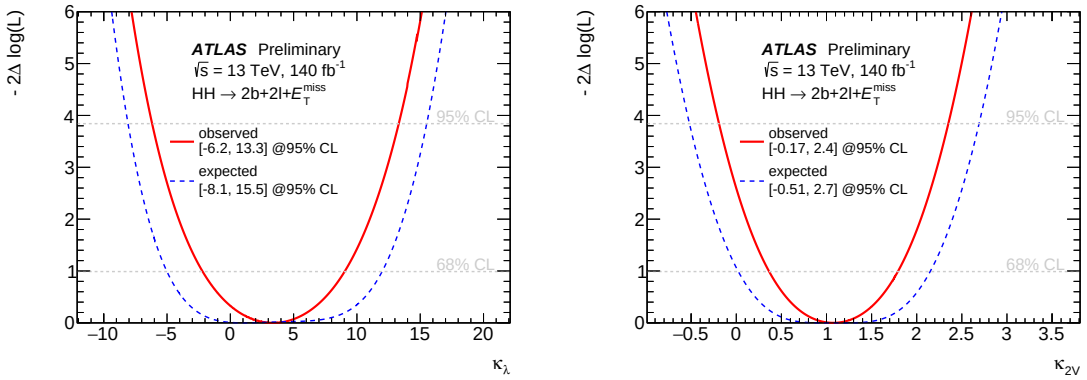

(a) (b)

Figure 7: Likelihood profiles of (a) the κ_λ and (b) κ_{2V} parameters.

9 Conclusion

A search for non-resonant Higgs boson pair production via the ggF and VBF production modes is performed. It probes decay channels with one of the Higgs bosons decaying to bb and the other to either WW^*, ZZ^*, or $\tau^+\tau^-$. Selected events contain exactly two b-tagged jets, two light leptons with opposite electric charge and missing transverse energy. The analysis employs 140 fb^{-1} of pp collision data at $\sqrt{s} = 13$ TeV, recorded by the ATLAS detector at the LHC. The results are consistent with the predictions for the SM background processes. An observed (expected) 95% CL upper limit on the cross-section for the production of Higgs boson pairs is set at 9.6 (16.2) times the SM prediction, which is a significant improvement compared to the previous ATLAS search in this channel which reported an observed (expected) 95% CL upper limit of 40 (29) [25]. The analysis also establishes a 95% CL limit on the Higgs coupling parameters κ_λ and κ_{2V} excluding values outside the ranges $[-6.2, 13.3]$ and $[-0.17, 2.4]$, respectively. These ranges are obtained under the assumption that all other couplings, except the individual coupling being tested, are set to their SM values.

Acknowledgements

We thank CERN for the very successful operation of the LHC, as well as the support staff from our institutions without whom ATLAS could not be operated efficiently.

We acknowledge the support of ANPCyT, Argentina; YerPhI, Armenia; ARC, Australia; BMWFW and FWF, Austria; ANAS, Azerbaijan; CNPq and FAPESP, Brazil; NSERC, NRC and CFI, Canada; CERN; ANID, Chile; CAS, MOST and NSFC, China; Minciencias, Colombia; MEYS CR, Czech Republic; DNRF and DNSRC, Denmark; IN2P3-CNRS and CEA-DRF/IRFU, France; SRNSFG, Georgia; BMBF, HGF and MPG, Germany; GSRI, Greece; RGC and Hong Kong SAR, China; ISF and Benoziyo Center, Israel; INFN, Italy; MEXT and JSPS, Japan; CNRST, Morocco; NWO, Netherlands; RCN, Norway; MEiN, Poland; FCT, Portugal; MNE/IFA, Romania; MESTD, Serbia; MSSR, Slovakia; ARRS and MIZŠ, Slovenia; DSI/NRF, South Africa; MICINN, Spain; SRC and Wallenberg Foundation, Sweden; SERI, SNSF and Cantons of Bern and Geneva, Switzerland; MOST, Taiwan; TENMAK, Türkiye; STFC, United Kingdom; DOE and

NSF, United States of America. In addition, individual groups and members have received support from BCKDF, CANARIE, Compute Canada and CRC, Canada; PRIMUS 21/SCI/017 and UNCE SCI/013, Czech Republic; COST, ERC, ERDF, Horizon 2020 and Marie Skłodowska-Curie Actions, European Union; Investissements d'Avenir Labex, Investissements d'Avenir Idex and ANR, France; DFG and AvH Foundation, Germany; Herakleitos, Thales and Aristeia programmes co-financed by EU-ESF and the Greek NSRF, Greece; BSF-NSF and MINERVA, Israel; Norwegian Financial Mechanism 2014-2021, Norway; NCN and NAWA, Poland; La Caixa Banking Foundation, CERCA Programme Generalitat de Catalunya and PROMETEO and GenT Programmes Generalitat Valenciana, Spain; Göran Gustafssons Stiftelse, Sweden; The Royal Society and Leverhulme Trust, United Kingdom.

The crucial computing support from all WLCG partners is acknowledged gratefully, in particular from CERN, the ATLAS Tier-1 facilities at TRIUMF (Canada), NDGF (Denmark, Norway, Sweden), CC-IN2P3 (France), KIT/GridKA (Germany), INFN-CNAF (Italy), NL-T1 (Netherlands), PIC (Spain), ASGC (Taiwan), RAL (UK) and BNL (USA), the Tier-2 facilities worldwide and large non-WLCG resource providers. Major contributors of computing resources are listed in Ref. [134].

References

[1] F. Englert and R. Brout, *Broken Symmetry and the Mass of Gauge Vector Mesons*, Phys. Rev. Lett. **13** (1964) 321, ed. by J. C. Taylor.

[2] P. W. Higgs, *Broken symmetries, massless particles and gauge fields*, Phys. Lett. **12** (1964) 132.

[3] P. W. Higgs, *Broken Symmetries and the Masses of Gauge Bosons*, Phys. Rev. Lett. **13** (1964) 508, ed. by J. C. Taylor.

[4] G. S. Guralnik, C. R. Hagen and T. W. B. Kibble, *Global Conservation Laws and Massless Particles*, Phys. Rev. Lett. **13** (1964) 585, ed. by J. C. Taylor.

[5] P. W. Higgs, *Spontaneous Symmetry Breakdown without Massless Bosons*, Phys. Rev. **145** (1966) 1156.

[6] T. W. B. Kibble, *Symmetry Breaking in Non-Abelian Gauge Theories*, Phys. Rev. **155** (1967) 1554, ed. by J. C. Taylor.

[7] ATLAS Collaboration, *Observation of a new particle in the search for the Standard Model Higgs boson with the ATLAS detector at the LHC*, Phys. Lett. B **716** (2012) 1, arXiv: 1207.7214 [hep-ex].

[8] CMS Collaboration, *Observation of a new boson at a mass of 125 GeV with the CMS experiment at the LHC*, Phys. Lett. B **716** (2012) 30, arXiv: 1207.7235 [hep-ex].

[9] S. Dawson, S. Dittmaier and M. Spira, *Neutral Higgs boson pair production at hadron colliders: QCD corrections*, Phys. Rev. D **58** (1998) 115012, arXiv: hep-ph/9805244.

[10] S. Borowka et al., *Higgs Boson Pair Production in Gluon Fusion at Next-to-Leading Order with Full Top-Quark Mass Dependence*, Phys. Rev. Lett. **117** (2016) 012001, [Erratum: Phys.Rev.Lett. 117, 079901 (2016)], arXiv: 1604.06447 [hep-ph].

[11] J. Baglio et al., *Gluon fusion into Higgs pairs at NLO QCD and the top mass scheme*, Eur. Phys. J. C **79** (2019) 459, arXiv: 1811.05692 [hep-ph].

[12] D. de Florian and J. Mazzitelli, *Higgs Boson Pair Production at Next-to-Next-to-Leading Order in QCD*, Phys. Rev. Lett. **111** (2013) 201801, arXiv: 1309.6594 [hep-ph].

[13] D. Y. Shao, C. S. Li, H. T. Li and J. Wang, *Threshold resummation effects in Higgs boson pair production at the LHC*, JHEP **07** (2013) 169, arXiv: 1301.1245 [hep-ph].

[14] D. de Florian and J. Mazzitelli, *Higgs pair production at next-to-next-to-leading logarithmic accuracy at the LHC*, JHEP **09** (2015) 053, arXiv: 1505.07122 [hep-ph].

[15] M. Grazzini et al., *Higgs boson pair production at NNLO with top quark mass effects*, JHEP **05** (2018) 059, arXiv: 1803.02463 [hep-ph].

[16] J. Baglio et al., $gg \to HH$*: Combined uncertainties*, Phys. Rev. D **103** (2021) 056002, arXiv: 2008.11626 [hep-ph].

[17] F. A. Dreyer and A. Karlberg, *Vector-Boson Fusion Higgs Pair Production at* N^3LO, Phys. Rev. D **98** (2018) 114016, arXiv: 1811.07906 [hep-ph].

[18] L. Di Luzio, R. Gröber and M. Spannowsky, *Maxi-sizing the trilinear Higgs self-coupling: how large could it be?*, Eur. Phys. J. C **77** (2017) 788, arXiv: 1704.02311 [hep-ph].

[19] G. D. Kribs, A. Maier, H. Rzehak, M. Spannowsky and P. Waite, *Electroweak oblique parameters as a probe of the trilinear Higgs boson self-interaction*, Phys. Rev. D **95** (2017) 093004, arXiv: 1702.07678 [hep-ph].

[20] ATLAS Collaboration, *Search for Higgs boson pair production in the two bottom quarks plus two photons final state in pp collisions at $\sqrt{s}$ = 13 TeV with the ATLAS detector*, Phys. Rev. D **106** (2021) 052001, arXiv: 2112.11876 [hep-ex].

[21] ATLAS Collaboration, *Search for resonant pair production of Higgs bosons in the $b\bar{b}b\bar{b}$ final state using pp collisions at $\sqrt{s}$ = 13 TeV with the ATLAS detector*, Phys. Rev. D **105** (2022) 092002, arXiv: 2202.07288 [hep-ex].

[22] ATLAS Collaboration, *Search for resonant and non-resonant Higgs boson pair production in the $b\bar{b}\tau^+\tau^-$ decay channel using 13 TeV pp collision data from the ATLAS detector*, JHEP **07** (2022) 040, arXiv: 2209.10910 [hep-ex].

[23] ATLAS Collaboration, *Constraining the Higgs boson self-coupling from single- and double-Higgs production with the ATLAS detector using pp collisions at $\sqrt{s}$ = 13 TeV*, Phys. Lett. B **843** (2022) 137745, arXiv: 2211.01216 [hep-ex].

[24] CMS Collaboration, *A portrait of the Higgs boson by the CMS experiment ten years after the discovery*, Nature **607** (2022) 60, arXiv: 2207.00043 [hep-ex].

[25] ATLAS Collaboration, *Search for non-resonant Higgs boson pair production in the $bb\ell\nu\ell\nu$ final state with the ATLAS detector in pp collisions at $\sqrt{s}$ = 13 TeV*, Phys. Lett. B **801** (2020) 135145, arXiv: 1908.06765 [hep-ex].

[26] ATLAS Collaboration, *The ATLAS Experiment at the CERN Large Hadron Collider*, JINST **3** (2008) S08003.

[27] ATLAS Collaboration, *ATLAS Insertable B-Layer: Technical Design Report*, ATLAS-TDR-19; CERN-LHCC-2010-013, 2010, URL: https://cds.cern.ch/record/1291633, Addendum: ATLAS-TDR-19-ADD-1; CERN-LHCC-2012-009, 2012, URL: https://cds.cern.ch/record/1451888.

[28] B. Abbott et al., *Production and integration of the ATLAS Insertable B-Layer*, JINST **13** (2018) T05008, arXiv: 1803.00844 [physics.ins-det].

[29] ATLAS Collaboration, *Performance of the ATLAS trigger system in 2015*, Eur. Phys. J. C **77** (2017) 317, arXiv: 1611.09661 [hep-ex].

[30] ATLAS Collaboration, *The ATLAS Collaboration Software and Firmware*, ATL-SOFT-PUB-2021-001, 2021, URL: https://cds.cern.ch/record/2767187.

[31] ATLAS Collaboration, *ATLAS data quality operations and performance for 2015–2018 data-taking*, JINST **15** (2020) P04003, arXiv: 1911.04632 [physics.ins-det].

[32] ATLAS Collaboration, *Luminosity determination in pp collisions at $\sqrt{s}$ = 13 TeV using the ATLAS detector at the LHC*, (2022), arXiv: 2212.09379 [hep-ex].

[33] ATLAS Collaboration, *The ATLAS Simulation Infrastructure*, Eur. Phys. J. C **70** (2010) 823, arXiv: 1005.4568 [physics.ins-det].

[34] S. Agostinelli et al., *GEANT4 – a simulation toolkit*, Nucl. Instrum. Meth. A **506** (2003) 250.

[35] T. Sjöstrand, S. Mrenna and P. Skands, *A brief introduction to PYTHIA 8.1*, Comput. Phys. Commun. **178** (2008) 852, arXiv: 0710.3820 [hep-ph].

[36] NNPDF Collaboration, R. D. Ball et al., *Parton distributions with LHC data*, Nucl. Phys. B **867** (2013) 244, arXiv: 1207.1303 [hep-ph].

[37] ATLAS Collaboration, *The Pythia 8 A3 tune description of ATLAS minimum bias and inelastic measurements incorporating the Donnachie–Landshoff diffractive model*, ATL-PHYS-PUB-2016-017, 2016, URL: https://cds.cern.ch/record/2206965.

[38] T. Sjöstrand et al., *An introduction to PYTHIA 8.2*, Comput. Phys. Commun. **191** (2015) 159, arXiv: 1410.3012 [hep-ph].

[39] J. Butterworth et al., *PDF4LHC recommendations for LHC Run II*, J. Phys. G **43** (2016) 023001, arXiv: 1510.03865 [hep-ph].

[40] ATLAS Collaboration, *ATLAS Pythia 8 tunes to 7 TeV data*, ATL-PHYS-PUB-2014-021, 2014, URL: https://cds.cern.ch/record/1966419.

[41] D. J. Lange, *The EvtGen particle decay simulation package*, Nucl. Instrum. Meth. A **462** (2001) 152.

[42] J. Bellm et al., *Herwig 7.2 release note*, Eur. Phys. J. C **80** (2020) 452, arXiv: 1912.06509 [hep-ph].

[43] ATLAS Collaboration, *Combination of searches for Higgs boson pairs in pp collisions at $\sqrt{s}$ = 13 TeV with the ATLAS detector*, Phys. Lett. B **800** (2020) 135103, arXiv: 1906.02025 [hep-ex].

[44] ATLAS Collaboration, *Validation of signal Monte Carlo event generation in searches for Higgs boson pairs with the ATLAS detector*, ATL-PHYS-PUB-2019-007, 2019, URL: https://cds.cern.ch/record/2665057.

[45] J. Alwall et al., *The automated computation of tree-level and next-to-leading order differential cross sections, and their matching to parton shower simulations*, JHEP **07** (2014) 079, arXiv: 1405.0301 [hep-ph].

[46] The NNPDF Collaboration, R. D. Ball et al., *Parton distributions for the LHC run II*, JHEP **04** (2015) 040, arXiv: 1410.8849 [hep-ph].

[47] F. Bishara, R. Contino and J. Rojo, *Higgs pair production in vector-boson fusion at the LHC and beyond*, Eur. Phys. J. C **77** (2017) 481, arXiv: 1611.03860 [hep-ph].

[48] ATLAS Collaboration, *Probing the Quantum Interference between Singly and Doubly Resonant Top-Quark Production in pp Collisions at $\sqrt{s}$ = 13 TeV with the ATLAS Detector*, Phys. Rev. Lett. **121** (2018) 152002, arXiv: 1806.04667 [hep-ex].

[49] S. Frixione, E. Laenen, P. Motylinski, C. White and B. R. Webber, *Single-top hadroproduction in association with a W boson*, JHEP **07** (2008) 029, arXiv: 0805.3067 [hep-ph].

[50] S. Frixione, G. Ridolfi and P. Nason, *A positive-weight next-to-leading-order Monte Carlo for heavy flavour hadroproduction*, JHEP **09** (2007) 126, arXiv: 0707.3088 [hep-ph].

[51] P. Nason, *A new method for combining NLO QCD with shower Monte Carlo algorithms*, JHEP **11** (2004) 040, arXiv: hep-ph/0409146.

[52] S. Frixione, P. Nason and C. Oleari, *Matching NLO QCD computations with parton shower simulations: the POWHEG method*, JHEP **11** (2007) 070, arXiv: 0709.2092 [hep-ph].

[53] S. Alioli, P. Nason, C. Oleari and E. Re, *A general framework for implementing NLO calculations in shower Monte Carlo programs: the POWHEG BOX*, JHEP **06** (2010) 043, arXiv: 1002.2581 [hep-ph].

[54] ATLAS Collaboration, *Studies on top-quark Monte Carlo modelling for Top2016*, ATL-PHYS-PUB-2016-020, 2016, URL: https://cds.cern.ch/record/2216168.

[55] L. Serkin, *Treatment of top-quark backgrounds in extreme phase spaces: the "top p_T reweighting" and novel data-driven estimations in ATLAS and CMS*, Proceeding for 13th International Workshop on Top Quark Physics, 2021, arXiv: 2105.03977 [hep-ex].

[56] E. Re, *Single-top Wt-channel production matched with parton showers using the POWHEG method*, Eur. Phys. J. C **71** (2011) 1547, arXiv: 1009.2450 [hep-ph].

[57] E. Bothmann et al., *Event generation with Sherpa 2.2*, SciPost Phys. **7** (2019) 034, arXiv: 1905.09127 [hep-ph].

[58] L. Lönnblad, *Correcting the Colour-Dipole Cascade Model with Fixed Order Matrix Elements*, JHEP **05** (2002) 046, arXiv: hep-ph/0112284.

[59] N. Lavesson and L. Lönnblad, *W+jets matrix elements and the dipole cascade*, JHEP **07** (2005) 054, arXiv: hep-ph/0503293.

[60] T. Gleisberg and S. Höche, *Comix, a new matrix element generator*, JHEP **12** (2008) 039, arXiv: 0808.3674 [hep-ph].

[61] F. Cascioli, P. Maierhöfer and S. Pozzorini, *Scattering Amplitudes with Open Loops*, Phys. Rev. Lett. **108** (2012) 111601, arXiv: 1111.5206 [hep-ph].

[62] S. Höche, F. Krauss, M. Schönherr and F. Siegert, *QCD matrix elements + parton showers. The NLO case*, JHEP **04** (2013) 027, arXiv: 1207.5030 [hep-ph].

[63] A. Djouadi, J. Kalinowski and M. Spira, *HDECAY: A program for Higgs boson decays in the Standard Model and its supersymmetric extension*, Comput. Phys. Commun. **108** (1998) 56, arXiv: hep-ph/9704448.

[64] M. Spira, *QCD Effects in Higgs Physics*, Fortsch. Phys. **46** (1998) 203, arXiv: hep-ph/9705337.

[65] A. Djouadi, M. M. Mühlleitner and M. Spira, *Decays of Supersymmetric particles: The Program SUSY-HIT (SUspect-SdecaY-Hdecay-InTerface)*, Acta Phys. Polon. B **38** (2007) 635, arXiv: hep-ph/0609292.

[66] A. Bredenstein, A. Denner, S. Dittmaier and M. M. Weber, *Radiative corrections to the semileptonic and hadronic Higgs-boson decays $H \to WW/ZZ \to 4$ fermions*, JHEP **02** (2007) 080, arXiv: hep-ph/0611234.

[67] A. Bredenstein, A. Denner, S. Dittmaier and M. M. Weber, *Precise predictions for the Higgs-boson decay $H \to WW/ZZ \to 4$ leptons*, Phys. Rev. D **74** (2006) 013004, arXiv: hep-ph/0604011 [hep-ph].

[68] A. Bredenstein, A. Denner, S. Dittmaier and M. M. Weber, *Precision calculations for the Higgs decays $H \to ZZ/WW \to 4$ leptons*, Nucl. Phys. Proc. Suppl. **160** (2006) 131, arXiv: hep-ph/0607060 [hep-ph].

[69] K. Hamilton, P. Nason, E. Re and G. Zanderighi, *NNLOPS simulation of Higgs boson production*, JHEP **10** (2013) 222, arXiv: 1309.0017 [hep-ph].

[70] K. Hamilton, P. Nason and G. Zanderighi, *Finite quark-mass effects in the NNLOPS POWHEG+MiNLO Higgs generator*, JHEP **05** (2015) 140, arXiv: 1501.04637 [hep-ph].

[71] K. Hamilton, P. Nason and G. Zanderighi, *MINLO: multi-scale improved NLO*, JHEP **10** (2012) 155, arXiv: 1206.3572 [hep-ph].

[72] J. M. Campbell et al., *NLO Higgs boson production plus one and two jets using the POWHEG BOX, MadGraph4 and MCFM*, JHEP **07** (2012) 092, arXiv: 1202.5475 [hep-ph].

[73] K. Hamilton, P. Nason, C. Oleari and G. Zanderighi, *Merging H/W/Z + 0 and 1 jet at NLO with no merging scale: a path to parton shower + NNLO matching*, JHEP **05** (2013) 082, arXiv: 1212.4504 [hep-ph].

[74] S. Catani and M. Grazzini, *Next-to-Next-to-Leading-Order Subtraction Formalism in Hadron Collisions and its Application to Higgs-boson Production at the Large Hadron Collider*, Phys. Rev. Lett. **98** (2007) 222002, arXiv: hep-ph/0703012 [hep-ph].

[75] ATLAS Collaboration, *Measurement of the Z/γ^* boson transverse momentum distribution in pp collisions at $\sqrt{s} = 7$ TeV with the ATLAS detector*, JHEP **09** (2014) 145, arXiv: 1406.3660 [hep-ex].

[76] D. de Florian et al., *Handbook of LHC Higgs Cross Sections: 4. Deciphering the Nature of the Higgs Sector*, (2016), arXiv: 1610.07922 [hep-ph].

[77] C. Anastasiou et al., *High precision determination of the gluon fusion Higgs boson cross-section at the LHC*, JHEP **05** (2016) 058, arXiv: 1602.00695 [hep-ph].

[78] C. Anastasiou, C. Duhr, F. Dulat, F. Herzog and B. Mistlberger, *Higgs Boson Gluon-Fusion Production in QCD at Three Loops*, Phys. Rev. Lett. **114** (2015) 212001, arXiv: 1503.06056 [hep-ph].

[79] F. Dulat, A. Lazopoulos and B. Mistlberger, *iHixs 2 – Inclusive Higgs cross sections*, Comput. Phys. Commun. **233** (2018) 243, arXiv: 1802.00827 [hep-ph].

[80] R. V. Harlander and K. J. Ozeren, *Finite top mass effects for hadronic Higgs production at next-to-next-to-leading order*, JHEP **11** (2009) 088, arXiv: 0909.3420 [hep-ph].

[81] R. V. Harlander and K. J. Ozeren, *Top mass effects in Higgs production at next-to-next-to-leading order QCD: Virtual corrections*, Phys. Lett. B **679** (2009) 467, arXiv: 0907.2997 [hep-ph].

[82] R. V. Harlander, H. Mantler, S. Marzani and K. J. Ozeren, *Higgs production in gluon fusion at next-to-next-to-leading order QCD for finite top mass*, Eur. Phys. J. C **66** (2010) 359, arXiv: 0912.2104 [hep-ph].

[83] A. Pak, M. Rogal and M. Steinhauser, *Finite top quark mass effects in NNLO Higgs boson production at LHC*, JHEP **02** (2010) 025, arXiv: 0911.4662 [hep-ph].

[84] S. Actis, G. Passarino, C. Sturm and S. Uccirati, *NLO electroweak corrections to Higgs boson production at hadron colliders*, Phys. Lett. B **670** (2008) 12, arXiv: 0809.1301 [hep-ph].

[85] S. Actis, G. Passarino, C. Sturm and S. Uccirati, *NNLO computational techniques: The cases $H \to \gamma\gamma$ and $H \to gg$*, Nucl. Phys. B **811** (2009) 182, arXiv: 0809.3667 [hep-ph].

[86] M. Bonetti, K. Melnikov and L. Tancredi, *Higher order corrections to mixed QCD-EW contributions to Higgs boson production in gluon fusion*, Phys. Rev. D **97** (2018) 056017, arXiv: 1801.10403 [hep-ph], Erratum: Phys. Rev. D **97** (2018) 099906(E).

[87] P. Nason and C. Oleari, *NLO Higgs boson production via vector-boson fusion matched with shower in POWHEG*, JHEP **02** (2010) 037, arXiv: 0911.5299 [hep-ph].

[88] M. Ciccolini, A. Denner and S. Dittmaier, *Strong and Electroweak Corrections to the Production of a Higgs Boson + 2 Jets via Weak Interactions at the Large Hadron Collider*, Phys. Rev. Lett. **99** (2007) 161803, arXiv: 0707.0381 [hep-ph].

[89] M. Ciccolini, A. Denner and S. Dittmaier, *Electroweak and QCD corrections to Higgs production via vector-boson fusion at the CERN LHC*, Phys. Rev. D **77** (2008) 013002, arXiv: 0710.4749 [hep-ph].

[90] P. Bolzoni, F. Maltoni, S.-O. Moch and M. Zaro, *Higgs Boson Production via Vector-Boson Fusion at Next-to-Next-to-Leading Order in QCD*, Phys. Rev. Lett. **105** (2010) 011801, arXiv: 1003.4451 [hep-ph].

[91] M. L. Ciccolini, S. Dittmaier and M. Krämer, *Electroweak radiative corrections to associated WH and ZH production at hadron colliders*, Phys. Rev. D **68** (2003) 073003, arXiv: hep-ph/0306234 [hep-ph].

[92] O. Brein, A. Djouadi and R. Harlander, *NNLO QCD corrections to the Higgs-strahlung processes at hadron colliders*, Phys. Lett. B **579** (2004) 149, arXiv: hep-ph/0307206.

[93] O. Brein, R. V. Harlander, M. Wiesemann and T. Zirke, *Top-quark mediated effects in hadronic Higgs-Strahlung*, Eur. Phys. J. C **72** (2012) 1868, arXiv: 1111.0761 [hep-ph].

[94] L. Altenkamp, S. Dittmaier, R. V. Harlander, H. Rzehak and T. J. E. Zirke, *Gluon-induced Higgs-strahlung at next-to-leading order QCD*, JHEP **02** (2013) 078, arXiv: 1211.5015 [hep-ph].

[95] A. Denner, S. Dittmaier, S. Kallweit and A. Mück, *HAWK 2.0: A Monte Carlo program for Higgs production in vector-boson fusion and Higgs strahlung at hadron colliders*, Comput. Phys. Commun. **195** (2015) 161, arXiv: 1412.5390 [hep-ph].

[96] O. Brein, R. V. Harlander and T. J. E. Zirke, *vh@nnlo – Higgs Strahlung at hadron colliders*, Comput. Phys. Commun. **184** (2013) 998, arXiv: 1210.5347 [hep-ph].

[97] R. V. Harlander, A. Kulesza, V. Theeuwes and T. Zirke, *Soft gluon resummation for gluon-induced Higgs Strahlung*, JHEP **11** (2014) 082, arXiv: 1410.0217 [hep-ph].

[98] H. B. Hartanto, B. Jäger, L. Reina and D. Wackeroth, *Higgs boson production in association with top quarks in the POWHEG BOX*, Phys. Rev. D **91** (2015) 094003, arXiv: 1501.04498 [hep-ph].

[99] ATLAS Collaboration, *Vertex Reconstruction Performance of the ATLAS Detector at* $\sqrt{s} = 13$ *TeV*, ATL-PHYS-PUB-2015-026, 2015, URL: https://cds.cern.ch/record/2037717.

[100] ATLAS Collaboration, *Electron and photon performance measurements with the ATLAS detector using the 2015–2017 LHC proton–proton collision data*, JINST **14** (2019) P12006, arXiv: 1908.00005 [hep-ex].

[101] ATLAS Collaboration, *Muon reconstruction performance of the ATLAS detector in proton–proton collision data at* $\sqrt{s} = 13$ *TeV*, Eur. Phys. J. C **76** (2016) 292, arXiv: 1603.05598 [hep-ex].

[102] ATLAS Collaboration, *Muon reconstruction and identification efficiency in ATLAS using the full Run 2 pp collision data set at* $\sqrt{s} = 13$ *TeV*, Eur. Phys. J. C **81** (2021) 578, arXiv: 2012.00578 [hep-ex].

[103] M. Cacciari, G. P. Salam and G. Soyez, *The anti-k_t jet clustering algorithm*, JHEP **04** (2008) 063, arXiv: 0802.1189 [hep-ph].

[104] M. Cacciari, G. P. Salam and G. Soyez, *FastJet user manual*, Eur. Phys. J. C **72** (2012) 1896, arXiv: 1111.6097 [hep-ph].

[105] ATLAS Collaboration, *Topological cell clustering in the ATLAS calorimeters and its performance in LHC Run 1*, Eur. Phys. J. C **77** (2017) 490, arXiv: 1603.02934 [hep-ex].

[106] ATLAS Collaboration, *Properties of jets and inputs to jet reconstruction and calibration with the ATLAS detector using proton–proton collisions at* $\sqrt{s} = 13$ *TeV*, ATL-PHYS-PUB-2015-036, 2015, URL: https://cds.cern.ch/record/2044564.

[107] ATLAS Collaboration, *Jet reconstruction and performance using particle flow with the ATLAS Detector*, Eur. Phys. J. C **77** (2017) 466, arXiv: 1703.10485 [hep-ex].

[108] ATLAS Collaboration, *Jet energy scale measurements and their systematic uncertainties in proton–proton collisions at $\sqrt{s}$ = 13 TeV with the ATLAS detector*, Phys. Rev. D **96** (2017) 072002, arXiv: 1703.09665 [hep-ex].

[109] ATLAS Collaboration, *Selection of jets produced in* 13 *TeV proton–proton collisions with the ATLAS detector*, ATLAS-CONF-2015-029, 2015, URL: https://cds.cern.ch/record/2037702.

[110] ATLAS Collaboration, *ATLAS flavour-tagging algorithms for the LHC Run 2 pp collision dataset*, Eur. Phys. J. C **83** (2022) 681, arXiv: 2211.16345 [physics.data-an].

[111] ATLAS Collaboration, *Performance of missing transverse momentum reconstruction with the ATLAS detector using proton–proton collisions at $\sqrt{s}$ = 13 TeV*, Eur. Phys. J. C **78** (2018) 903, arXiv: 1802.08168 [hep-ex].

[112] M. Cacciari and G. P. Salam, *Pileup subtraction using jet areas*, Phys. Lett. B **659** (2008) 119, arXiv: 0707.1378 [hep-ph].

[113] F. Chollet et al., *Keras*, 2015, URL: https://keras.io.

[114] M. Abadi et al., *TensorFlow: Large-scale Machine Learning on Heterogeneous Systems*, Software available from tensorflow.org, 2015, URL: https://www.tensorflow.org/.

[115] L. Breiman, *Random Forests*, Machine Learning **45** (2001) 5.

[116] T. Akiba, S. Sano, T. Yanase, T. Ohta and M. Koyama, *Optuna: A Next-generation Hyperparameter Optimization Framework*, 2019, arXiv: 1907.10902 [cs.LG].

[117] A. L. Read, *Presentation of search results: the CL_S technique*, J. Phys. G **28** (2002) 2693.

[118] V. Nair and G. E. Hinton, *Rectified Linear Units Improve Restricted Boltzmann Machines*, Proceedings of the 27th International Conference on International Conference on Machine Learning, 2010.

[119] C. G. Lester and D. J. Summers, *Measuring masses of semi-invisibly decaying particles pair produced at hadron colliders*, Phys. Lett. B **463** (1999) 99, arXiv: hep-ph/9906349.

[120] C. G. Lester and B. Nachman, *Bisection-based asymmetric M_{T2} computation: a higher precision calculator than existing symmetric methods*, JHEP **03** (2015) 100, arXiv: 1411.4312 [hep-ph].

[121] ATLAS Collaboration, *Object-based missing transverse momentum significance in the ATLAS Detector*, ATLAS-CONF-2018-038, 2018, URL: https://cds.cern.ch/record/2630948.

[122] A. Hoecker et al., *TMVA - Toolkit for Multivariate Data Analysis*, 2007, arXiv: physics/0703039 [physics.data-an].

[123] J. Erdmann et al., *A likelihood-based reconstruction algorithm for top-quark pairs and the KLFitter framework*, Nucl. Instrum. Meth. A **748** (2014) 18, arXiv: 1312.5595 [hep-ex].

[124] A. Elagin, P. Murat, A. Pranko and A. Safonov, *A new mass reconstruction technique for resonances decaying to $\tau\tau$*, Nucl. Instrum. Meth. A **654** (2011) 481, arXiv: 1012.4686 [hep-ex].

[125] CMS Collaboration, *Measurement of the cross section and angular correlations for associated production of a Z boson with b hadrons in pp collisions at $\sqrt{s}$ = 7 TeV*, JHEP **12** (2013) 039, arXiv: 1310.1349 [hep-ex].

[126] ATLAS Collaboration, *Measurement of differential production cross-sections for a Z boson in association with b-jets in* 7 *TeV proton–proton collisions with the ATLAS detector*, JHEP **10** (2014) 141, arXiv: 1407.3643 [hep-ex].

[127] ATLAS Collaboration, *Jet Calibration and Systematic Uncertainties for Jets Reconstructed in the ATLAS Detector at* $\sqrt{s}$ = 13 *TeV*, ATL-PHYS-PUB-2015-015, 2015, URL: https://cds.cern.ch/record/2037613.

[128] G. Avoni et al., *The new LUCID-2 detector for luminosity measurement and monitoring in ATLAS*, JINST **13** (2018) P07017.

[129] ATLAS Collaboration, *Simulation of top-quark production for the ATLAS experiment at* $\sqrt{s}$ = 13 *TeV*, ATL-PHYS-PUB-2016-004, 2016, URL: https://cds.cern.ch/record/2120417.

[130] S. Höche, F. Krauss, S. Schumann and F. Siegert, *QCD matrix elements and truncated showers*, JHEP **05** (2009) 053, arXiv: 0903.1219 [hep-ph].

[131] S. Catani, F. Krauss, B. R. Webber and R. Kuhn, *QCD Matrix Elements + Parton Showers*, JHEP **11** (2001) 063, arXiv: hep-ph/0109231.

[132] ATLAS Collaboration, *Combined search for the Standard Model Higgs boson in* pp *collisions at* $\sqrt{s}$ = 7 *TeV with the ATLAS detector*, Phys. Rev. D **86** (2012) 032003, arXiv: 1207.0319 [hep-ex].

[133] G. Cowan, K. Cranmer, E. Gross and O. Vitells, *Asymptotic formulae for likelihood-based tests of new physics*, Eur. Phys. J. C **71** (2011) 1554, arXiv: 1007.1727 [physics.data-an], Erratum: Eur. Phys. J. C **73** (2013) 2501.

[134] ATLAS Collaboration, *ATLAS Computing Acknowledgements*, ATL-SOFT-PUB-2023-001, 2023, URL: https://cds.cern.ch/record/2869272.